JOURNAL OF MATERIALS SCIENCE 26 (1991) 2731–2742

Fibre orientation and mechanical behaviour in reinforced thermoplastic injection mouldings

M. AKAY, D. BARKLEY
Department of Mechanical and Industrial Engineering, University of Ulster at Jordanstown, Newtownabbey, Co. Antrim BT37 0QB, UK

Process variables, fibre orientation distribution and mechanical properties were inter-related for injection-moulded short-glass fibre-reinforced polypropylene and polyamide and long-glass fibre-reinforced polyamide. The properties of the reinforced grades were also contrasted with those of the base polymer. A rectangular mould with triple pin-edge gates on the same side to facilitate a single melt flow-front or double flow-front advancing adjacently, was employed. Mouldings were evaluated for fibre orientation distribution, and tensile, dynamic mechanical and fracture properties. The relative magnitudes of the shell and the core fibre-orientation persuasions depended on the melt and the mould temperatures, and the injection ram speed. An increase in G_c, K_c, ultimate tensile strength (UTS) and elastic moduli values and a decrease in $\tan\delta$ values were observed with fibre reinforcement. The properties showed marked sensitivity to the position of the specimens in the moulding because of the associated variations in the fibre orientation. The prediction of UTS based on a rule of mixture relationship for strength and the Halpin–Tsai equations for elastic moduli had limited success. The predictions were improved by employing measured data representative of regions of high fibre orientation, e.g. knit-line. The estimation was weakened in the material systems containing significant production-induced voids. An inference of the fracture toughness values was that the composites contained flows of the order of 0.2 mm in size, which is conceivable, either as voids or as defects introduced in the machining of the specimens.

1. Introduction

The advantages conferred on polymeric matrices through fibre reinforcement are well established. In the case of injection-moulded discontinuous-fibre-reinforced thermoplastics, however, a realistic assessment can only be made taking due account of processing and tooling variables. There is a marked interaction between processing parameters and induced fibre orientation distribution. Furthermore, knit-lines and boundary layers assume greater significance in reinforced thermoplastics. These factors have been well covered for short-fibre-reinforced thermoplastics with up to 33% by weight loadings [1–10]. However, there is comparatively little work [1, 6, 7, 11] on both short (< 1 mm) and long (< 10 mm) fibre-reinforced thermoplastics, at higher loading levels. It is important that the rheological, structural and mechanical performance relationships should be verified as fibre length and/or fibre content increases. Accordingly, the work presented here examined injection-moulded short-glass fibre-reinforced polypropylene and polyamide with up to 50% by weight fibre content and attempted to interrelate process variables, material structure and mechanical properties.

The layered nature of fibre distribution through the thickness of a moulding and the position dependency of this distribution was assessed by scanning electron microscopy (SEM).

The tensile, dynamic mechanical and impact properties of the mouldings with respect to fibre orientation distribution were determined using representative test-pieces. The measurements from different tests were correlated and those of ultimate tensile strength (UTS) were also compared with the predictions based on a modified rule of mixtures relationship.

2. Experimental procedure

2.1. Materials and processing

The details of the materials used are given in Table I.

Plaques of 3.6 mm × 73 mm × 150 mm were prepared employing a Stubbe SKM51 injection-moulding machine and a mould with triple pin-edge gates (1 mm × 6 mm) situated on the same side to facilitate a single melt flow-front or double flow-fronts advancing adjacently, see Fig. 1.

The machine was set at 13 MPa hydraulic pressure, 0.7 MPa back pressure, 80 rev min^{-1} screw speed, 50 mm s^{-1} ram forward speed, and a barrel temperature profile of 220, 230, 240, 250 °C for polypropylenes and 260, 270, 280, 290 °C for polyamides. The mould surface temperature was normally 40 °C for polypropylenes and 80 °C for polyamides.

Some filled polyamide plaques were produced at 10 and 25 mm s^{-1} ram speeds; 270, 280, 290, 300 °C and

0022–2461/91 $03.00 + .12

TABLE I

Description	Identification	ICI Grade
Unfilled polypropylene	PP	GWM 22
30% short-fibre polypropylene	SFRPP30	HW160GR 30
Unfilled polyamide	PA	Maranyl A100
50% short-fibre polyamide	SFRPA50	Maranyl A690
50% long-fibre polyamide	LFRPA50	Verton RF70010

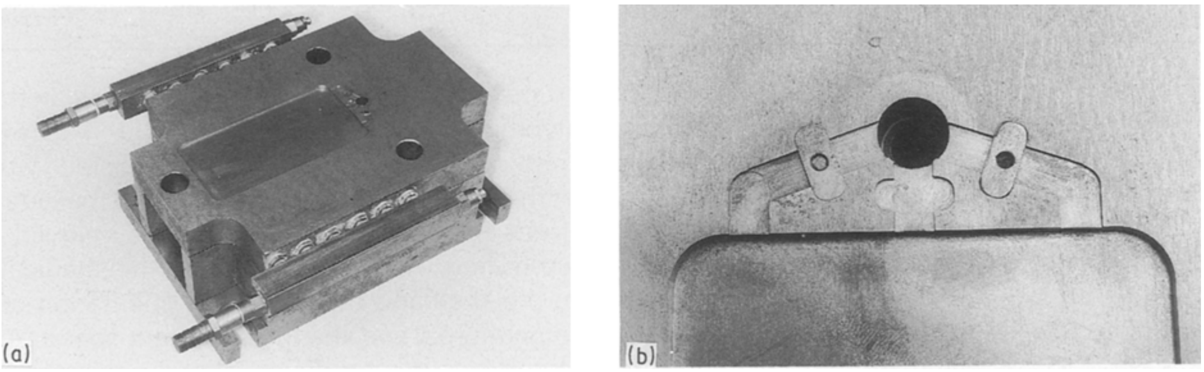

Figure 1 (a) The mould and (b) a close-up of the gates.

280, 290, 300, 310 °C barrel profiles; and 60, 90 and 100 °C mould temperatures.

All polyamide-based raw materials were dried in a vacuum oven at 95 °C for 4 h prior to processing. Once moulded, all the plaques were immediately placed in sealed impermeable bags with silica-gel desiccant, until required for testing.

2.2. Test methods

Tensile tests were conducted in accordance with ASTM D638M, at 5 mm min^{-1}, and the results quoted represent an average of at least five measurements. Dumb-bell-shaped specimens of 6 mm width and 33 mm gauge length were cut with a high-speed router; transverse (T) and longitudinal (L) to the mould-fill direction and representing different locations in the moulding as shown in Fig. 2. The tests were conducted at ambient with approximately 20 °C temperature and 60% relative humidity.

The moisture content of the test-pieces was determined by weighing before and after drying under vacuum at 80 °C for 24 h, indicating approximately 0.4% and 0.2% moisture in unfilled and filled polyamides, respectively.

Dynamic properties were determined by means of Du Pont DMA employed in fixed frequency mode. Specimens (3.6 mm × 10 mm × 30 mm) were tested at 1 Hz and a temperature sweep rate of 4 °C min^{-1}. The sinusoidal oscillation amplitude was set at 0.4 mm and the Poisson's ratios assumed to be 0.4.

Impact tests were performed in a three-point loading mode on a 40 mm span and using an instrumented falling weight machine at 1 m s^{-1} impact speed. Bars of approximately 73 mm length and 10 mm depth were milled with a 45°, 0.25 mm radius cutter in a range of notch depth to bar depth ratios from

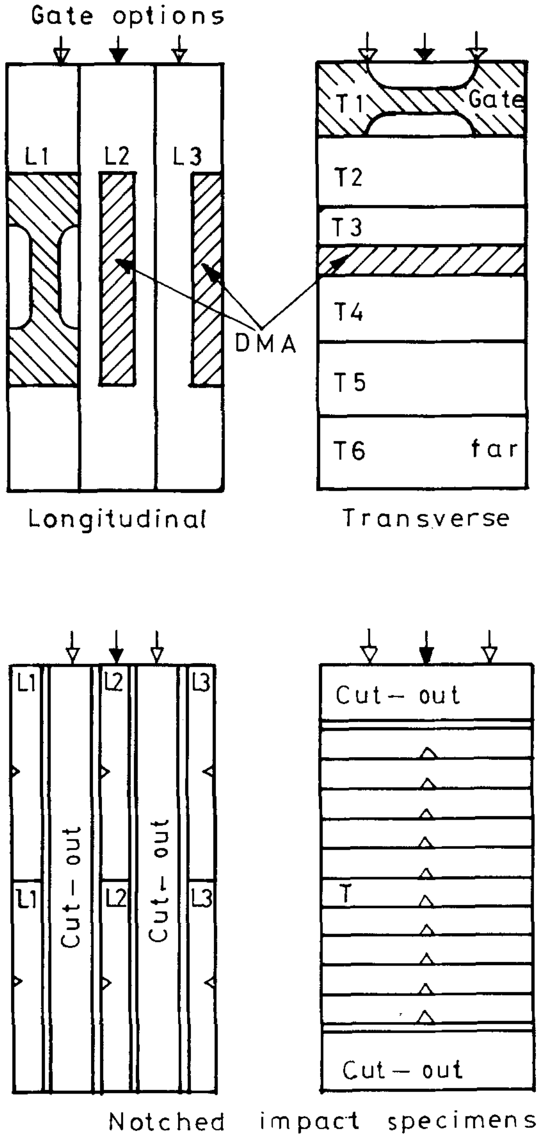

Figure 2 Tensile, DMA and impact specimen locations (→ single gated; → double gated).

0.03–0.45 and impacted on edge. The fracture properties, G_c and K_c, were determined from typically triangular force–deflection impact failure traces and using the analysis based on an energy calibration factor, Φ, and a stress intensity calibration factor, Y [12, 13], so that

$$G_c = U/(BD\Phi) \quad (1)$$

and

$$K_c^2 = Y^2\sigma^2 a \quad (2)$$

where U is the energy absorbed to failure and σ is the failure stress. B, D and a are the breadth, depth and notch depth, respectively, of the specimen. Φ and Y are function of a/D.

Fibre orientation distribution was estimated by ordinary photography and SEM. The core of the plaques, because of specific fibre orientation, appeared whiter and was conveniently measured from photographs taken at a low magnification (×4). Detailed study of fibre orientation was conducted by SEM, employing a Joel-35 scanner. Sufficiently polished and gold-coated specimens taken from various locations in the plaque were scanned and scanning electron micrographs were prepared.

The distribution of fibre content through the thickness of the mouldings was evaluated by pyrolysis. Microtomed slivers from known depths in the plaque were initially dried in a vacuum oven at 95 °C for 1 h, weighed and then placed in a furnace at 600 °C for 1 h to burn off the matrix in order to isolate and to determine the weight of the fibre ash.

3. Results and discussion

3.1. Fibre orientation distribution

Mouldings frequently comprise a layered structure distinguishable by changes in fibre orientation and/or concentration [4, 8, 9, 14]. Preferential fibre alignments and their magnitudes through the thickness of the moulding are induced by differential solidification, shearing, and melt-flow patterns (including divergence, convergence and the shape of the flow-fronts). In a simple mould cavity of the type considered here the fibre orientation is predominantly along the fill direction within a shell layer at all the mould surfaces, whereas the core consists of a predominantly transverse fibre alignment. The core was easily discernible in the cross-sections, Fig. 3, by a colour change where the core appeared whiter. This made it convenient to quantify the extent of coring. Scanning electron micrographs (Figs 4–8) of polished sections helped collaborate the core measurements and also clearly revealed a five-tiered fibre orientation distribution, i.e. skin/shell/core/shell/skin. The skin layer, comprising near random orientation was of the order of 5% and 7% of the thickness for polyamides and polypropylenes, respectively. The relative sizes of the shell and the core depended on the processing conditions as illustrated in Fig. 9. Further details have been presented elsewhere [15]. However, the standard process settings produced a core of 30%, the minimum settings 20% and the maximum settings 60%.

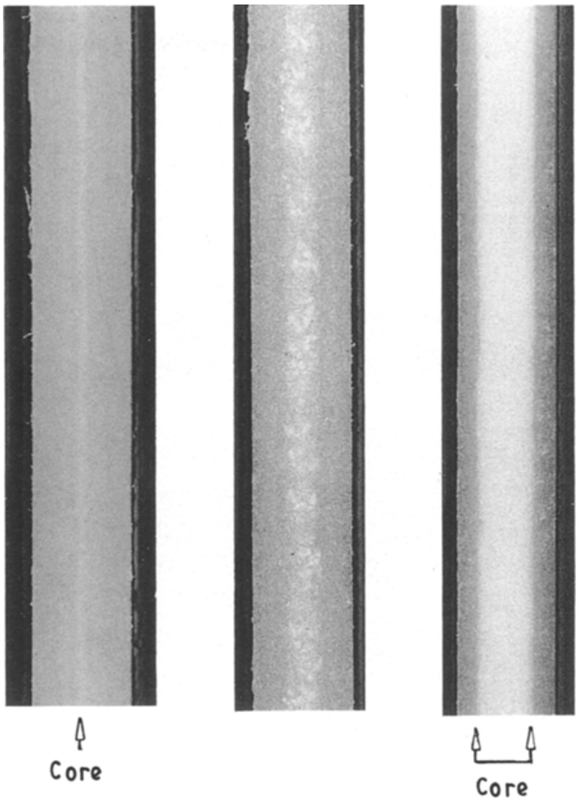

Figure 3 Plaque cross-sections showing various core thicknesses.

At the elevated temperature settings of 100 °C mould surface and 310 °C nozzle, the mouldings did not discolour. However, it should be pointed out that the extremes of conditions employed here lie outside the manufacturer's recommendations.

SEM work illustrated that the core began to feature only beyond 10 mm off the side-edges (Fig. 6) and developed in a gradual manner (cf. sections b and c in Figs 4 and 5 for core size). Scanning electron micrographs also clearly showed the presence of voids in the core of LFRPA50, which appears to get worse with increasing core thickness (cf. Fig. 4c with Fig. 5c). The voiding is accentuated because of a rather deep mould cavity where significant flow divergence occurs.

A high degree of fibre alignment existed parallel to the knit-line, Fig. 10, and spread over 8 mm on either side of the line.

Burn-off data showed a gradual fibre depletion from the core to the skin, Fig. 11. The fibre concentration was above the nominal weight level in the core and below this level in the shell by approximately 5% for SFRPA50 and 15% for LFRPA50.

3.2. Tensile behaviour

3.2.1. Influence of core-size

The influence of core-size on tensile properties is shown in Figs 12 and 13 for a longitudinal specimen. There was a clear reduction in UTS for both short- and long-fibre-reinforced polyamides with increasing core thickness. The effect on stiffness was less marked.

The measured values of UTS for 30% and 60% cores were compared with theoretical predictions based on a rule-of-mixtures expression for failure

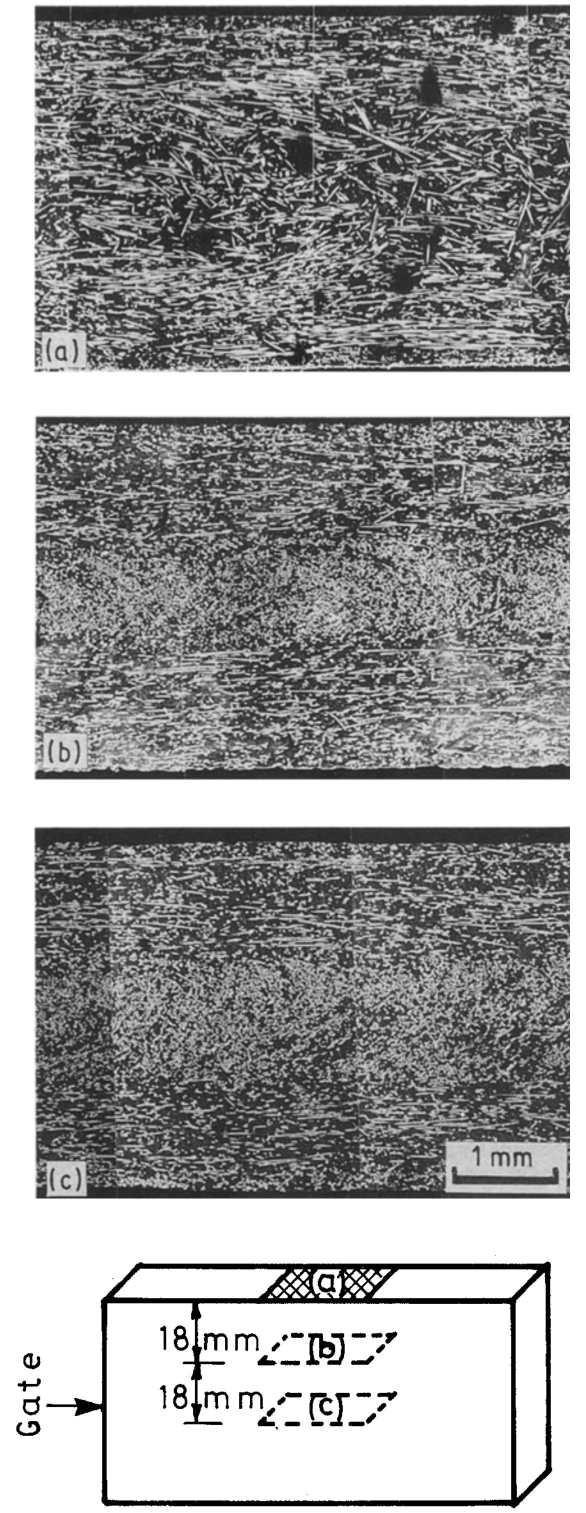

Figure 4 Scanning electron micrographs of LFRPA50: representative of regions a, b and c. The core measured 30% at c.

stresses

$$\sigma_C = \sigma_L A_L + \sigma_T A_T \tag{3}$$

where C, L and T represent the composite, the longitudinal layer and the transverse layer, respectively, and A represents the area fraction. Equation 3 can be expressed in terms of elastic moduli of the layers by assuming a uniform and elastic deformation. Therefore, the UTS for a specimen of unit width becomes

$$\sigma_{UC} = \sigma_{UL}[D_L + (E_T/E_L)D_T] \tag{4}$$

where D represents the layer depth fraction.

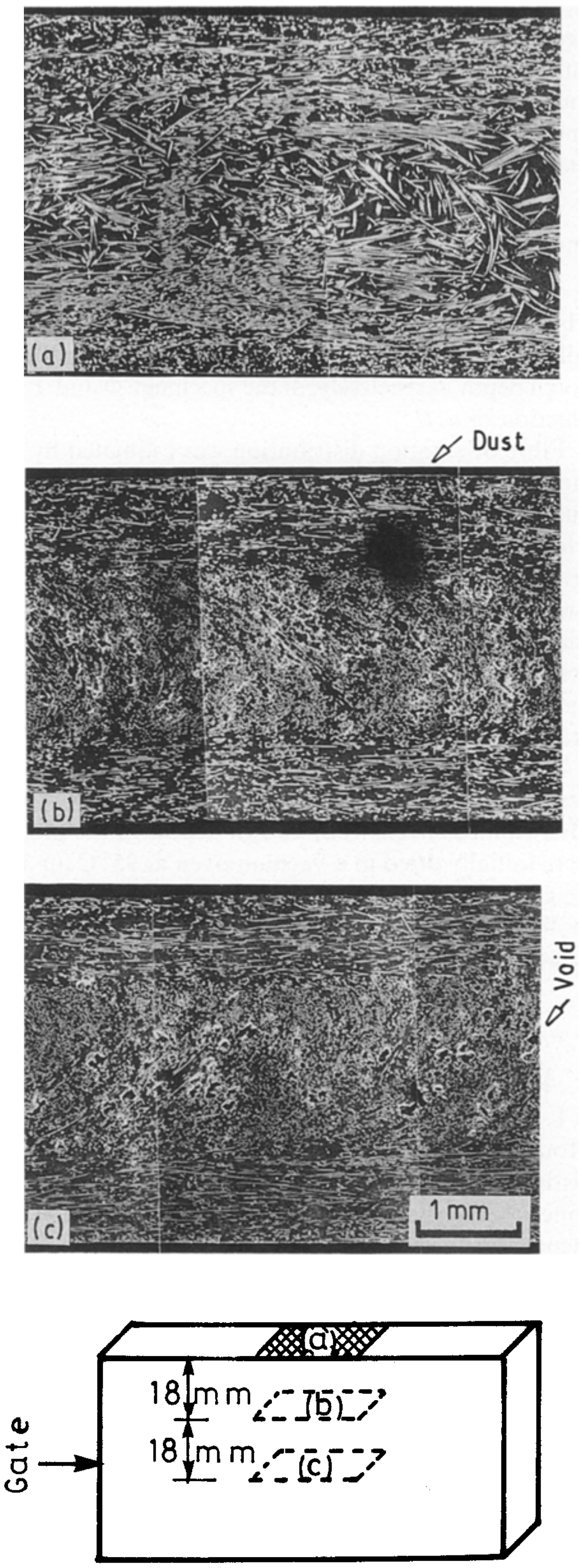

Figure 5 Scanning electron micrographs of LFRPA50; representative of regions a, b and c. The core measured 50% at c.

The random orientation of the skin was assumed to make equal contributions to the shells and the core, accordingly the core values were taken as 35% and 65%. Furthermore, the through-depth variation in the fibre concentration was included into the UTS estimation as below

$$\sigma_{UC} = \sigma_{UL}[D_L F_s + (E_T/E_L) D_T F_c] \tag{5}$$

where F_s and F_c are fibre-concentration factors for the shell and the core layers, respectively.

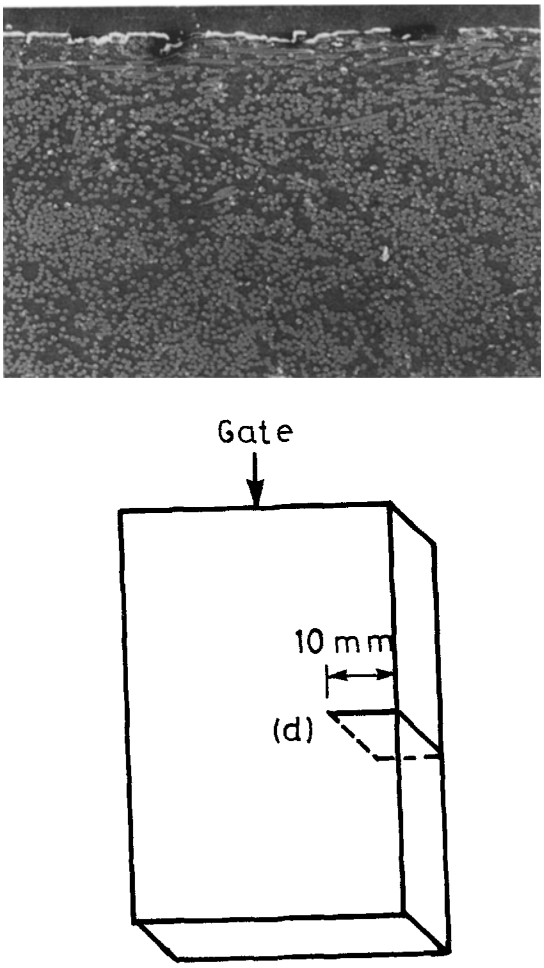

Figure 6 Scanning electron micrograph of LFRPA50: representative of region d.

The tensile strength, σ_{UL}, of the layer with fibres parallel to the tensile axis for $l < l_c$ is given by [16]

$$\sigma_{UL} = \frac{\tau l}{d} V_f + \sigma_m(1 - V_f) \quad (6)$$

where τ is the shear strength of the fibre–matrix interface, σ_m is the tensile strength of the matrix, l and d are the mean length and the diameter of the fibre, and V_f is the fibre volume fraction. By substituting the data given in Table II, σ_{UL} was estimated to be 320 MPa for SFRPA50 and 367 MPa for LFRPA50.

Longitudinal and transverse elastic moduli were estimated employing the Halpin–Tsai equations [17]

$$E_L/E_m = [1 + (2l/d)\eta_L V_f]/(1 - \eta_L V_f) \quad (7)$$

where

$$\eta_L = [(E_f/E_m) - 1]/[(E_f/E_m) + 2(l/d)] \quad (8)$$

$$E_T/E_m = (1 + \alpha\eta_T V_f)/(1 - \eta_T V_f) \quad (9)$$

where

$$\eta_T = [(E_f/E_m) - 1]/[(E_f/E_m) + \alpha] \quad (10)$$

The geometric factor $\alpha = 0.5$ for transverse orientation [18]. Substitution of the data (Table II) in the Halpin–Tsai equations produced $E_L = 16.4$ GPa for LFRPA50, $E_L = 15.7$ GPa for SFRPA50 and $E_T = 3.7$ GPa.

Further substitution of the estimated values of the elastic moduli and tensile strength into Equation 5 produced the UTS values shown in Table III (column A). The predicted values are around 1.5 times the measured values. In another study [19] on glass fibre-reinforced PET, the predicted tensile strengths have been found to be 2.5 times the observed values. The overestimation arises from the assumptions of uniform fibre alignment and of flaw-free mouldings in the equations employed.

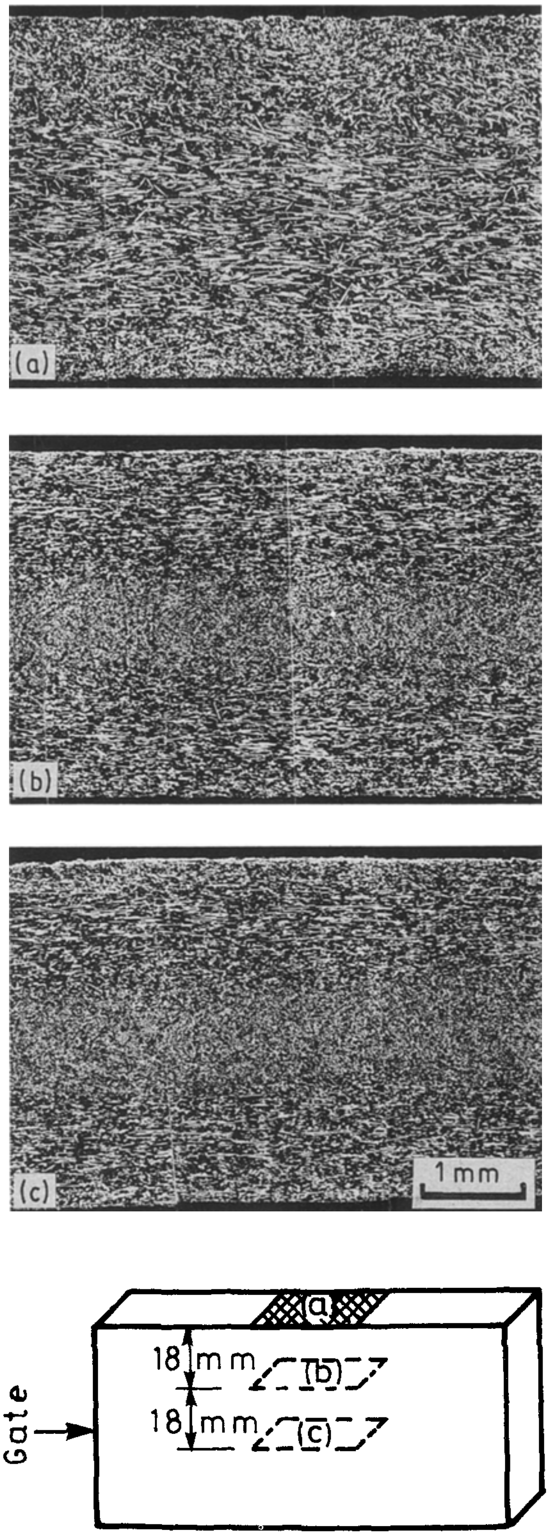

Figure 7 Scanning electron micrographs of SFRPA50: representative of regions a, b and c.

A more realistic estimate may be achieved by using measured values for σ_{UL}, E_L and E_T. Specimens taken along the knit-line (L2) were used to obtain values for

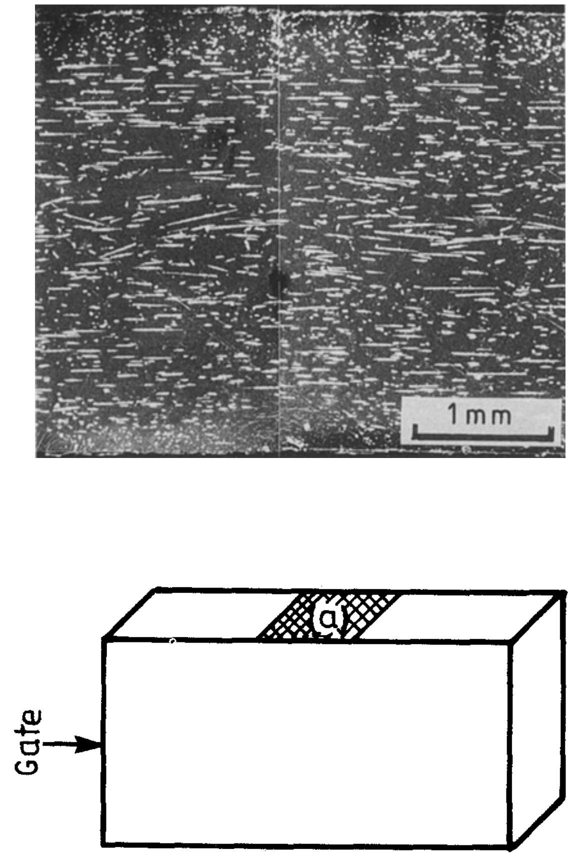

Figure 8 Scanning electron micrograph of SFRPP30: representative of region a.

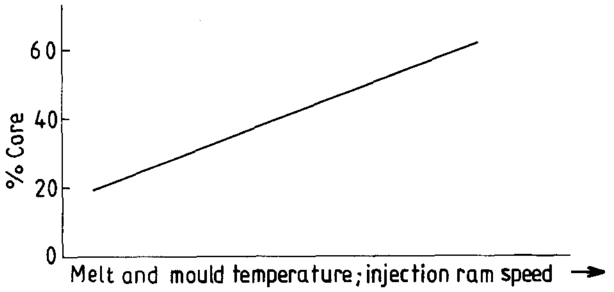

Figure 9 Schematic illustration of the influence of processing parameters on core size.

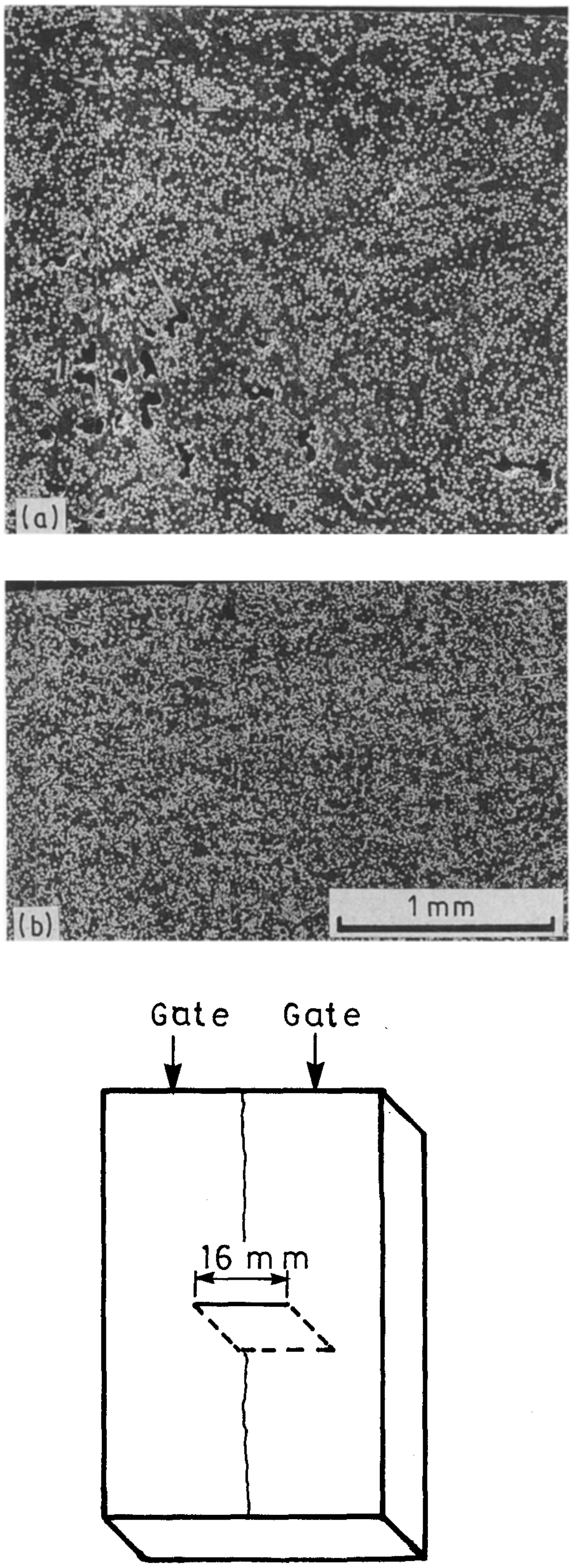

Figure 10 Scanning electron micrographs representative of the knit-line region. (a) LFRPA50, (b) SFRPA50.

σ_{UL} and E_L, and across the knit-line (T) for E_T. This approach was regarded to be appropriate because of the high degree of fibre alignment at the location of knit-line (see Fig. 10).

Substitution of the knit-line data (Table IV) in Equation 5 produced the estimated values presented in Table III (column B). These are much closer to the measured values, although not indicating the extent of drop experienced in UTS as core size was increased. Furthermore, the predicted values are on the whole higher than the measured ones, arising, perhaps, from the assumption that the longitudinal and the transverse layers both experience the same strain. This assumption can be avoided by basing the estimation solely on the strength values of the component layers, using the rule of mixtures relationship for stress (Equation 3), which may be re-expressed as

$$\sigma_{UC} = \sigma_{UL} D_L F_s + \sigma_{UT} D_T F_c \qquad (11)$$

The predictions presented in Table III (column C) were obtained from the knit-line data (Table IV) for σ_{UL} and σ_{UT}. These have close agreement with the observed UTS values for SFRPA50. The method underestimates the tensile strength of LFRPA50, due to lower than expected measured values for σ_{UL} and σ_{UT}, caused by voids. The estimation for LFRPA50 would improve considerably if based on data obtained

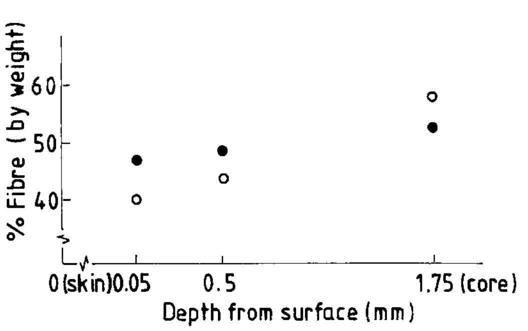

Figure 11 Fibre content through the thickness: (●) SFRPA50; (○) LFRPA50.

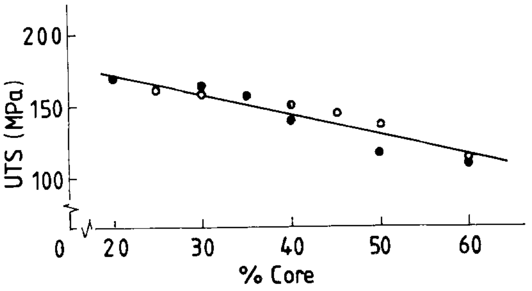

Figure 12 Core size versus UTS for specimens L2: (●) SFRPA50; (○) LFRPA50.

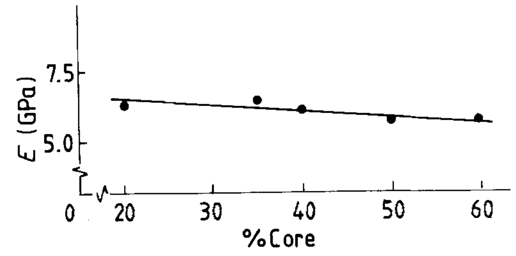

Figure 13 Core size versus elastic modulus for SFRPA50 at L2.

TABLE II Data for the rule-of-mixtures strength predictions

Property	SFRPA50	LFRPA50	Source
τ (MPa)	45	45	[20]
σ_m (MPa)	71	71	Measured
E_m (GPa)	2.3	2.3	Measured
E_f (GPa)	69	69	[21]
l (mm)	0.2	0.4	Measured
d (mm)	0.01	0.017	Measured
V_f	0.3	0.3	Manufacturer
D_T (thin core)	0.35	0.35	Measured
D_L (thick shell)	0.65	0.65	Measured
D_T (thick core)	0.65	0.65	Measured
D_L (thin shell)	0.35	0.35	Measured
F_s	0.95	0.85	Measured
F_c	1.05	1.15	Measured

from thinner mouldings, which suffer less from voiding.

3.2.2. Position dependence

Variation in the fibre orientation distribution was the main cause of the observed position dependence in tensile behaviour. Figs 14 and 15 show that the longitudinal specimens from the side edges of the moulding (L1 and L3), where the fill-direction fibre orientation predominates, had a higher UTS than those from the middle (L2) where across-the-fill alignment is most prominent. This behaviour was reversed when knit-lines were introduced into the mouldings. The

TABLE III Measured and predicted UTS values for reinforced polyamides

Material	Core fraction	UTS (MPa)			
		A	B	C	Measured
SFRPA50	0.35	226	174	160	164
SFRPA50	0.65	158	148	122	110
LFRPA50	0.35	236	156	140	160
LFRPA50	0.65	171	137	104	111

TABLE IV Measured knit-line data

Property	SFRPA50	LFRPA50
σ_{UL} (MPa)	216	210
σ_{UT} (MPa)	73	56
E_L (GPa)	8.5	9.0
E_T (GPa)	4.4	4.3

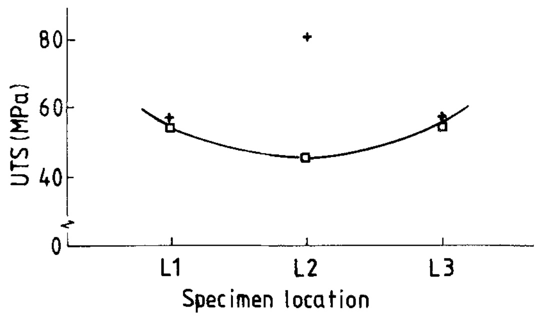

Figure 14 UTS at various specimen locations: (□) SFRPP30; (+) SFRPP30 (with knit-line).

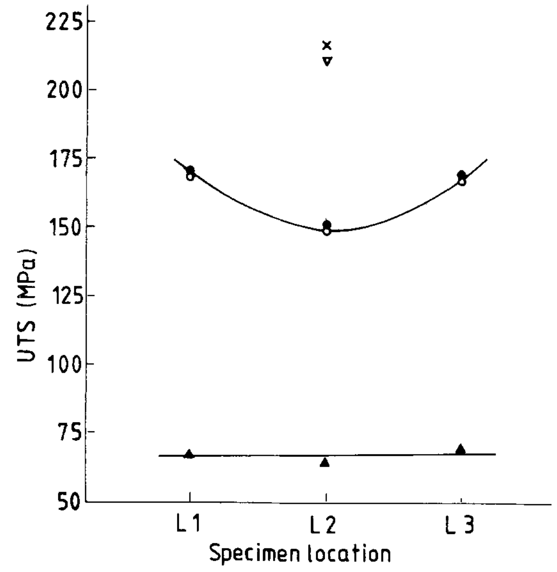

Figure 15 UTS at various specimen locations: (▲) PA; (●) SFRPA50; (○) LFRPA50; (×) SFRPA50 (knit-line); (▽) LFRPA50 (knit-line).

strength along the knit-line at the centre (L2) was dramatically higher than the edges, e.g. 216 MPa compared to 170 MPa for SFRPA50.

Transverse specimens (T1–T6) exhibited little position sensitivity except that the sample nearest the gate (T1) had a slightly lower UTS than the rest (Fig. 16). This can be explained by considering the situation when the cavity is almost completely filled. At this point any remaining melt which passes through the gate into the mould does not experience any divergence because the mould is almost filled. As a result the longitudinal fibre alignment, which predominates in the runner and gate, remains in the moulding near the gate. This localized region of longitudinally aligned fibres reduces the UTS for loads applied in a transverse direction. A more significant increase in UTS was expected at the end of the plaque (T6), where a flattening of the flow front causes more of the fibres to align orthogonally to the fill-direction.

3.3. Dynamic mechanical behaviour

The dynamic mechanical properties of E' and $\tan\delta$ over a wide range of temperature for polyamides are presented in Figs 17–19; note that where the $\tan\delta$ traces are identical, only one is shown for brevity. Fibre incorporation increased E' and produced a significantly shallow $\tan\delta$ peak at a higher temperature (see Fig. 19). The extent of reduction in $\tan\delta$ (a measure of damping in the material) was in excess of the magnitude of reduction in the polymer volume. Replacement of 30% polymer by fibre resulted in reduction of $\tan\delta$ peak height and the area under the $\tan\delta$ trace by over 60%. Fibres shield the matrix from some of the applied alternating stress, causing further reductions in the damping and displacing the transition point to a higher temperature. This has also been observed in the polypropylene grades [1, 22]. The influence of fibres is most pronounced when there is a high degree of fibre alignment in the direction of applied load. Accordingly, the specimen taken from the side-edge (L1) produced the highest modulus and the least damping. In comparison, the specimen (T) from across the knit-line produced moderate variations in the dynamic properties because of the transverse alignment of the fibres to the applied load at the knit-line.

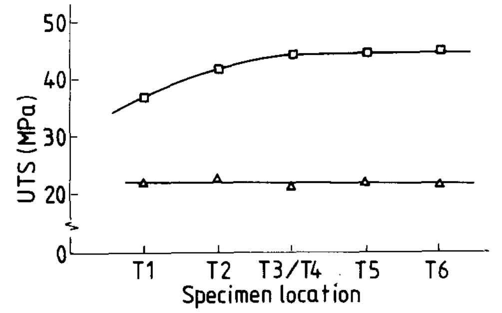

Figure 16 UTS at various specimen locations: (△) PP; (□) SFRPP30.

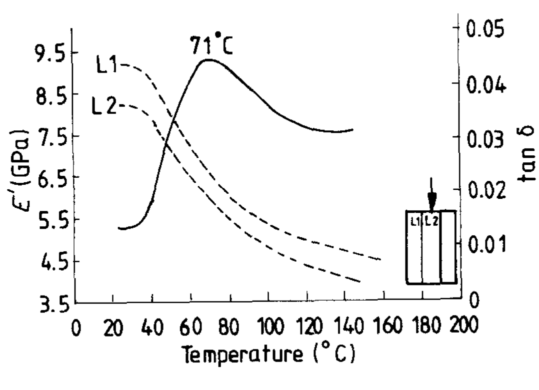

Figure 17 Dynamic mechanical properties for SFRPA50 at specimen locations L1 and L2. (---) E', (——) $\tan\delta$.

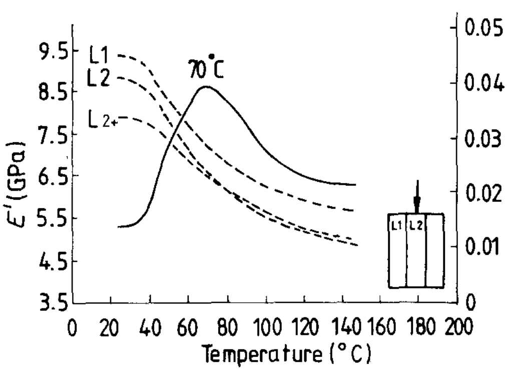

Figure 18 Dynamic mechanical properties for LFRPA50 at locations L1 and L2 (where specimen "L2 +" has a larger core). (---) E', (——) $\tan\delta$.

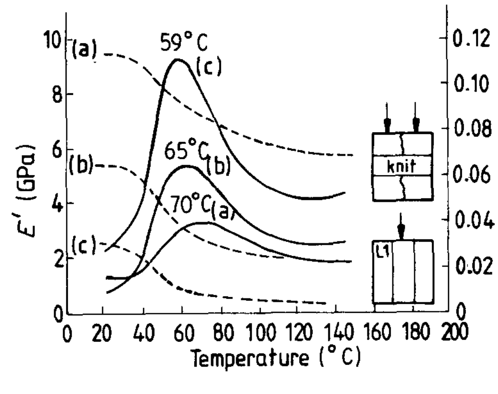

Figure 19 Dynamic mechanical properties for: (a) LFRPA50 at L1; (b) LFRPA50 across the knit-line; (c) PA at L1. (---) E', (——) $\tan\delta$.

The position-dependent response of the reinforced mouldings was, once again, in evidence as shown in Figs 17 and 18.

3.4. Fracture behaviour

Typical fracture data are presented in Figs 20–23 for filled and unfilled polyamides. The unfilled polyamide produced negative energy and stress intercepts and, therefore, the data were not employed in determining fracture properties, G_c and K_c. This, and other aspects of the fracture behaviour of such ductile polymers, has been covered in the literature (amongst others by Williams [23] and Vu-Khanh [24]).

The effect of fibre alignment is highlighted in Figs 22 and 23. The specimens taken from the edge of the plaque (L1) feature a high degree of longitudinal fibre

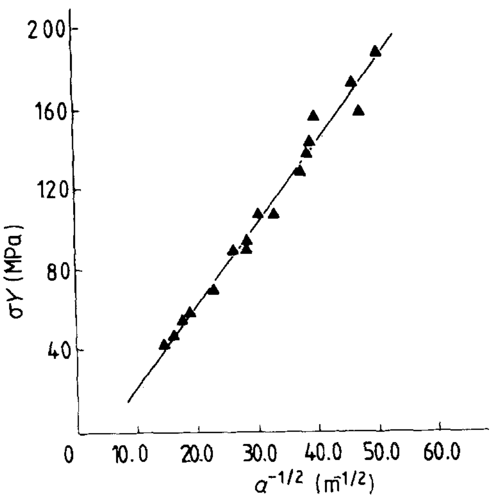

Figure 20 Fracture toughness data for PA.

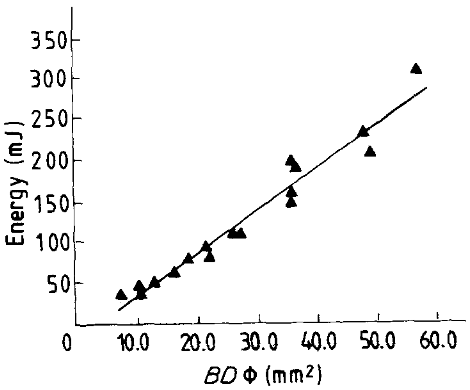

Figure 21 Fracture energy versus *BD*Φ for PA.

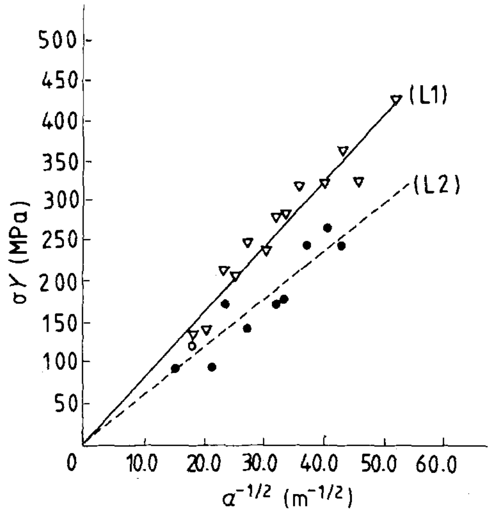

Figure 22 Fracture toughness data for SFRPA50 at locations L1 and L2.

alignment and so have higher values of K_c and G_c compared with those taken from the centre (L2) where significant transverse fibre alignment exists. Failure in the latter case is mainly due to debonding or interface failure whereas in the former, it is a mixture of fibre fracture and fibre pullout, resulting in the higher values for fracture toughness.

A linear correlation between K_c and the tensile strength, for a range of composites, mainly continuous fibre-reinforced thermosets, has been shown [25] to correspond to an intrinsic flaw size of 1 mm. In turn, it has been concluded that because this is unrealistic, K_c may be inappropriate for assessing these composites. In a similar approach, a graph of K_c versus UTS was drawn (Fig. 24) using the results (Table V) for the reinforced grades, and the ratio of K_c to UTS was found to be 0.044 $m^{1/2}$. Adapting the equation derived by Broek [26] for the plastic zone size, r_p, and substituting σ_y by UTS

$$r_p = \{K_c/[Y(\text{UTS})]\}^2/\pi \qquad (12)$$

where Y is the geometric calibration factor and is assumed to equal the average value (1.75) during the tests. Substituting 0.044 for the ratio of K_c/UTS, the flaw size was found to equal 0.2 mm. As a further check, a method was devised which relies on the assumption that all fracture data for a given material lie on a best-fit line. Thus the fracture data from an unnotched sample should also lie on this line.

Accordingly, the intrinsic flaw size was calculated as follows: using the fracture data for LFRPA50 (Fig. 25) a best-fit line was drawn, and the intersect of this line with the average fracture energy value for the unnotched specimens was taken to represent the *BD*Φ value for the intrinsic notch depth. The corresponding *a*/*D* ratio was obtained from the relationship shown in Fig. 26 and the flaw size estimated as 0.2 mm. It is reasonable to assume that the materials

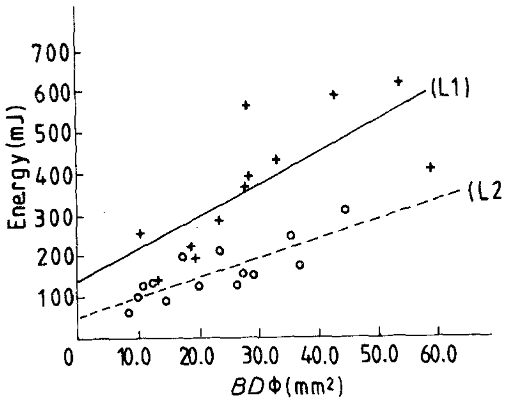

Figure 23 Fracture energy versus *BD*Φ for LFRPA50 at locations L1 and L2.

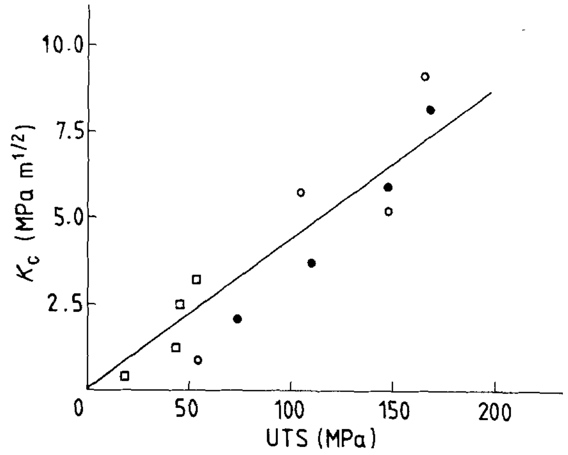

Figure 24 K_c versus UTS for: (□) SFRPP30; (●) SFRPA50; (○) LFRPA50.

TABLE V Mechanical properties

Material	Specimen position	K_c (MPa m$^{1/2}$)	G_c (kJ m^{-2})	UTS (MPa)	E (GPa) by various methods		
					LEFM	tensile	DMA
PP	T3	0.9	1.2	21	0.7	0.7	
PP	Knit-line (T3)	1.2	1.8	20	0.8	0.7	
SFRPP30	T3	1.2	1.3	44	1.1	1.6	
SFRPP30	Knit-line (T3)	0.4	0.4	20	0.4	0.7	
SFRPP30	L3	3.2	3.0	54	3.4	3.3	
SFRPP30	L2	2.5	1.7	46	3.7	2.6	
SFRPA50	T3	3.7	2.2	110	6.2	5.6	
SFRPA50	Knit-line (T3)	2.1	1.1	73	4.0	4.4	5.1
SFRPA50	L3	8.2	7.1	167	9.5	8.5	9.3
SFRPA50	L2	5.9	5.0	148	7.0	6.9	8.3
LFRPA50	T3	5.7	3.5	104	9.3	5.9	
LFRPA50	Knit-line (T3)	0.9	0.2	56	4.1	4.3	5.4
LFRPA50	L3	9.1	7.8	165	10.6	9.0	9.4
LFRPA50	L2	5.2	4.8	147	5.6	5.8	8.8

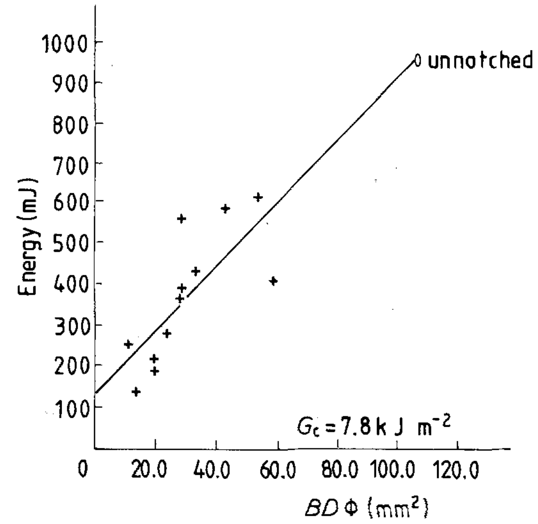

Figure 25 An estimation of the damage caused by machining.

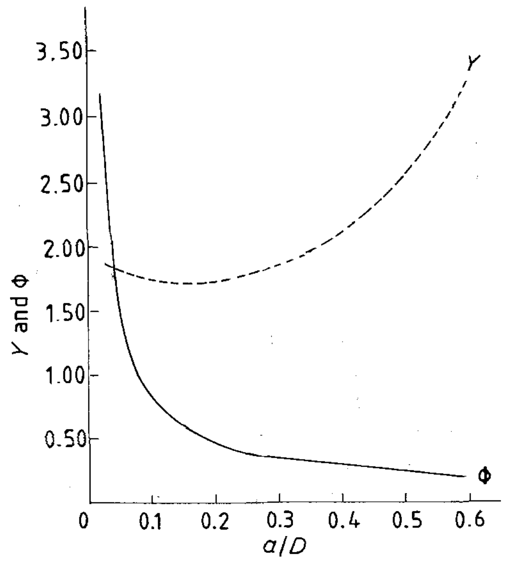

Figure 26 The variation of the calibration factors Y and Φ with notch depth ratio.

tested in this investigation could contain flaws of the order of 0.2 mm in length. These flaws could easily arise as a result of fibre dislodgement during the preparation of test-pieces and/or void formation during moulding. Therefore there seems no need to question the validity of the LEFM analysis on the grounds of intrinsic flaw size.

It has been suggested [27] that if these flaws become sufficiently large, some of the data points, with high $BD\Phi$ vlaues, could deviate from the best-fit line in a G_c graph. In this case a correction can be made by adding the estimated flaw size to the notch depths and re-plotting the graph. The G_c graph is more susceptible to the effects of flaw-size than the K_c graph. This is due to the shape of the calibration curves which are used in the analysis (Fig. 26). The calibration factor Φ changes rapidly with small changes in notch depth at lower values of a/D. This will cause significant errors in $BD\Phi$ if the effective notch, due to the addition of flaws, differs from the machined notch. This should be compared with the Y calibration factor which only becomes sensitive to variations in notch depth at higher values of a/D (> 0.5). Because these depths are not normally used in the analysis [13], the K_c graph remains largely unaffected.

Finally, the three methods of stiffness assessment are compared in Fig. 27 and Table V. The measured moduli (tensile and DMA) are plotted against the LEFM-derived modulus which is given by the relationship $E = K_c^2/G_c$. It can be seen that there is a reasonable correlation between the three methods and a best-fit line can be drawn. Some of the DMA results deviate from this line but these can be explained by a consideration of the mechanical configuration of the DMA test. The specimens which deviate are those which feature cores of transverse fibres. The DMA test applies a bending strain and the outer layers of the specimen experience most of the stress. Thus due to the load-bearing ability of the longitudinal fibre-containing outer layers, even specimens with large transverse cores sustain the stress more effectively and,

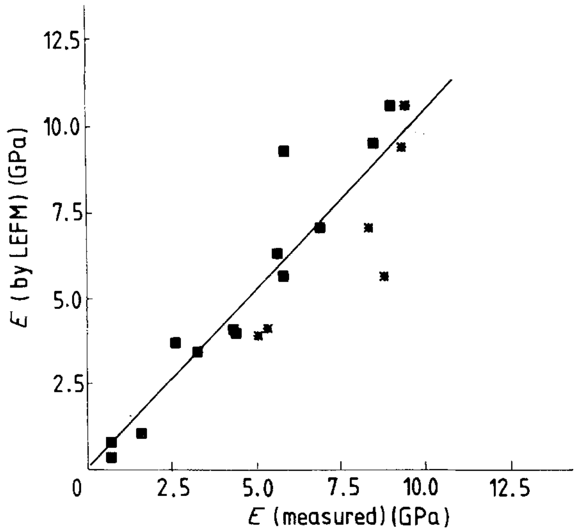

Figure 27 Derived elastic modulus (LEFM) versus the measured elastic moduli by (■) static tensile and (*) DMA.

as a result, exhibit a higher stiffness when tested by the DMA technique.

4. Conclusions

1. Fibre orientation distribution generates a multi-layered cross-section of random skin/longitudinal shell/transverse core/longitudinal shell/random skin. The skin layer ($\simeq$ 5% for the polyamides) appears to be independent of, whereas the shell and the core are strongly dependent on, the process variables. Higher mould surface and barrel profile temperatures, and faster injection ram speeds favour the formation of larger cores.

The core develops gradually from the side edges into the centre of the plaque, starting at approximately 10 mm from the edges.

2. Coring, as would be expected, causes a reduction in UTS along the mould-fill direction. The prediction of UTS based on rule of mixture relationships and Halpin–Tsai equations produces an overestimation. A more realistic estimation can be obtained, particularly for smaller cores, employing the knit-line data.

3. There is a gradual drop in the fibre concentration from the core to the skin: the variation from the nominal fibre content (50% by weight) being 5% for SFRPA50 and 15% for LFRPA50.

4. Variation in fibre orientation distribution across the moulding width has considerable effect on the mechanical properties: specimens representing the side edges (L1), where the longitudinal fibre arrangement predominates, exhibit superior properties over those representing the centre (L2), where transverse fibre alignment is significant. UTS improves by around 20% for the polypropylene and 40% for the polyamides, E' by 10% for the polyamides, and G_c and K_c by 40% for the short-fibre-reinforced polyamide and by over 60% for the long-fibre-reinforced polyamide.

5. Fibre incorporation causes stress-shielding of the matrix and thus increases T_g, and more significantly reduces damping beyond that possible by matrix volume reduction alone.

6. A linear correlation of K_c and UTS, and the inclusion of the data for unnotched specimens into G_c versus $BD\Phi$ regression, both indicate an inherent defect size of 0.2 mm. A defect of this magnitude can easily be introduced into these composites during the processing and/or specimen preparation. Accordingly, the application of the fracture mechanics does not lead to any unreasonable conclusion.

7. There is a good agreement between the elastic modulus values determined by static, dynamic and impact tests.

Acknowledgements

The financial support and the raw material provision by ICI Advanced Materials, Wilton, is much appreciated. The authors thank Drs R. S. Bailey and D. R. Moore, ICI, for their much valued cooperation and technical advice.

References

1. M. AKAY and D. BARKLEY, *Compos. Struct.* **3** (1985) 269.
2. G. AKAY, in "Developments in Injection Moulding—3", edited by A. Whelan and J. P. Goff (Elsevier Applied Science, Barking, Essex, 1985) pp. 271–316.
3. M. J. FOLKES, "Short Fibre Reinforced Thermoplastics" (Wiley, Letchworth, Herts, 1982).
4. P. F. BRIGHT and M. W. DARLINGTON, *Plast. Rubb. Process. Applic.* **1** (1981) 139.
5. M. G. BADER, in "Handbook of Composites", Vol. 4, "Fabrication of Composites", edited by A. Kelly and N. Yu. Rabotnov (Elsevier Science, Amsterdam, 1983) pp. 177–219.
6. A. C. GIBSON and A. N. McCLELLAND, in "Proceedings of IMechE Conference on Fibre Reinforced Composites" (Mechanical Engineering Publications Ltd, 1986) pp. 99–103.
7. G. CUFF, in "Proceedings of the 14th Reinforced Plastics Congress", Brighton, November 1984 (British Plastics Federation, 1984) paper 19, p. 79.
8. D. McNALLY, *Polym. Plast. Technol.* **8**(2) (1977) 101.
9. P. F. BRIGHT, R. J. CROWSON and M. J. FOLKES, *J. Mater. Sci.* **13** (1978) 2497.
10. J. KARGER-KOCIS and K. FRIEDRICH, *Plast. Rubb. Process. Applic.* **8**(2) (1987) 91.
11. R. S. BAILEY, M. DAVIES and D. R. MOORE, in "Proceedings of the 2nd International Conference on Testing, Evaluation and Quality Control of Composites", University of Surrey, Guildford, September 1987, edited by J. Herriot (Butterworths, Kent, 1987) p. 87.
12. E. PLATI and J. G. WILLIAMS, *Polym. Engng Sci.* **15** (1975) 470.
13. W. F. BROWN and J. E. STAWLEY, ASTM STP 410 (American Society for Testing and Materials, Philadelphia, Pennsylvania, 1966) pp. 1–66.
14. G. KALISKE and F. MEYER, *Plaste u Kant* **22** (1975) 496.
15. D. BARKLEY, PhD thesis, University of Ulster at Jordanstown, September 1989.
16. A. KELLY and W. R. TYSON, *J. Mech. Phys. of Solids* **6** (1965) 13.
17. J. C. HALPIN and S. W. TSAI, in Air Force Material Laboratory Technical Report, AFML-TR-67-423 (1967).
18. L. E. NIELSEN, "Mechanical Properties of Polymers and Composites", Vol. 2 (Marcel Dekker, New York, 1974) p. 459.
19. J. C. MALZAHN and J. M. SCHULTZ, *Compos. Sci. Technol.* **27** (1986) 253.

20. W. H. BOWYER and M. G. BADER, *J. Mater. Sci.* **7** (1972) 1315.
21. A. H. COTTRELL, "The Mechanical Properties of Matter" (Wiley, New York, 1964).
22. A. K. GUPTA, V. B. GUPTA, R. H. PETERS, W. G. HARLAND and J. P. BERRY, *J. Appl. Polym. Sci.* **27** (1982) 4669.
23. J. G. WILLIAMS, "Fracture Mechanics of Polymers" (Ellis Horwood, 1984).
24. T. Vu-KHANH, *Polymer* **29** (1988) 1979.
25. B. HARRIS, S. E. DOREY and R. G. COOKE, *Compos. Sci. Technol.* **31** (1988) 121.
26. D. BROEK, "Elementary Engineering Fracture Mechanics" (Martinus Nijhoff, Dordrecht, 1986).
27. M. AKAY and D. BARKLEY, *Polym. Test.* **7** (1987) 391.

Received 26 March
and accepted 19 July 1990